UV-photochemistry of the disulfide bond: Evolution of early photoproducts from picosecond X-ray absorption spectroscopy at the sulfur K-Edge

Miguel Ochmann,[a,‡] Abid Hussain,[a,‡] Inga von Ahnen,[a] Amy A. Cordones,[b] Kiryong Hong,[c] Jae Hyuk Lee,[b] Rory Ma,[c] Katrin Adamczyk,[a] Tae Kyu Kim,[c,*] Robert W. Schoenlein,[b,*] Oriol Vendrell,[d,*] and Nils Huse[a,*]

[a]*Department of Physics, University of Hamburg and Max Planck Institute for the Structure and Dynamics of Matter, Center for Free Electron Laser Science, 22761 Hamburg, Germany*

[b]*Ultrafast X-ray Science Lab, Chemical Sciences Division, Lawrence Berkeley National Laboratory, Berkeley, California 94720, USA*

[c]*Department of Chemistry and Chemistry Institute of Functional Materials, Pusan National University, Busan 46241, South Korea*

[d]*Center for Free-Electron Laser Science, DESY and The Hamburg Centre for Ultrafast Imaging, 22607 Hamburg, Germany*

[‡]The authors contributed equally to this work

Supporting information

Temporal modeling

Biexponential decay models were fit to the recorded time traces at the three probe energies of 2466.5 eV, 2467.4 eV, and 2471.5 eV. The temporal instrument response function is given by the duration of the Gaussian X-ray pulses (70 ps FWHM = $2\sigma\cdot\sqrt{[2\ln 2]}$) because the laser pulses are only 100 fs FWHM in duration. The temporal modelling is given by the convolution of the instrument response function and the response of dimethyl disulfide (DMDS) molecules which we approximate by:

$$\Delta A(E,t) = \{1+\mathrm{erf}[(t-t_0)/(\sqrt{2}\cdot\sigma)]\}/2 \cdot \ldots$$

$$\{A_1(E)\cdot\exp[(t-t_0)/\tau_1] + A_2(E)\cdot\exp[(t-t_0)/\tau_2] + A_3(E)\}.$$

This approximation is adequate because the X-ray pulse duration σ = 30 ps is much shorter than the observed time-evolution, τ_1 & τ_2, of the molecular system (for details see supporting information of reference [1]. In addition, we have modeled the pump-probe signals that are still present at the maximum measured time delay by $A_3(E)$ as the amplitude of the long-lived component. Fig. S1 shows short delay scans for the three indicated probe energies around zero delay. The fit curves with $2\sigma\cdot\sqrt{[2\ln 2]}$ = 70 ps are the same as in the main article but the measured data in Fig. S1 has smaller delay step sizes. The fit shows that the instrument response function is well described by the above model.

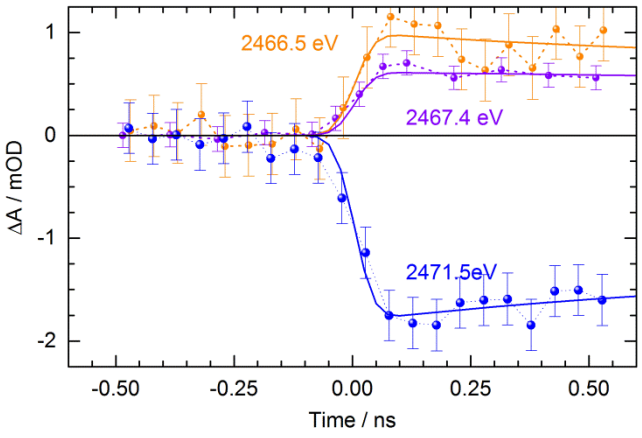

Figure S1. Delay scans at the three X-ray probe energies, indicated by color-coded arrows in Fig. 1B of the main article, show the growing-in of induced absorption (orange: 2466.5 eV, violet: 2467.4 eV) and ground-state bleaching (blue, 2471.5 eV) along with exponential decay models (solid lines) fit to the experimental data in Fig. 1B of the main article.

The strong radio frequency (RF) signals generated by the Pockels cell driver of the amplified laser system generated differential signals in the data acquisition system that were of a magnitude similar to the response of the molecular system to femtosecond UV excitation. This electronic laser signal typically rings for microseconds at sub-GHz

frequencies (~0.5 GHz at beamline 6.0.1) and required a good temporal electronic background characterization for use as a reference scan. Therefore, delay scans have been generated from the difference of ordinary pump-probe scans and background delay scans without X-rays impinging on the transmission intensity detector.

An example of such data sets is shown in panel A of Fig. S2 were the purple signal trace is the difference of the initial pump-probe signal (black solid circles) and the electronic laser background (grey open circles). Note that we have slightly rescaled the time scans in the main manuscript to adjust the signal changes of the delay scans to the signal changes of the energy scan. The changes per data point in the energy scans are taken in close succession of seconds and hence under exactly the same experimental conditions while the signal changes between delay scans vary, depending on exact laser power and spatial overlap before each scan. As laser power and spatial overlap drift slightly over the course of a day, they are readjusted every few hours, signal changes between delay scans may therefore vary by 10%. Nonetheless, error bars for each scan are fully valid because the relative noise and variation of each data point within a scan are comparable because they are taken in close succession of seconds.

Panels B and C of Figure S2 show the full data range to which the models were fit on a semi-logarithmic scale to better visualize the different timescales. In panel B individual fits where performed with only zero delay as a global fitting parameter. The width of the response function was known from the storage ring machine parameters of the Advanced Light Source (ALS). In the following two tables all parameters of the fits are displayed. Parameters are fixed when the standard error is zero. Starred parameters are formally shared. If they are actually shared depends on whether the amplitude of a component is fixed at zero.

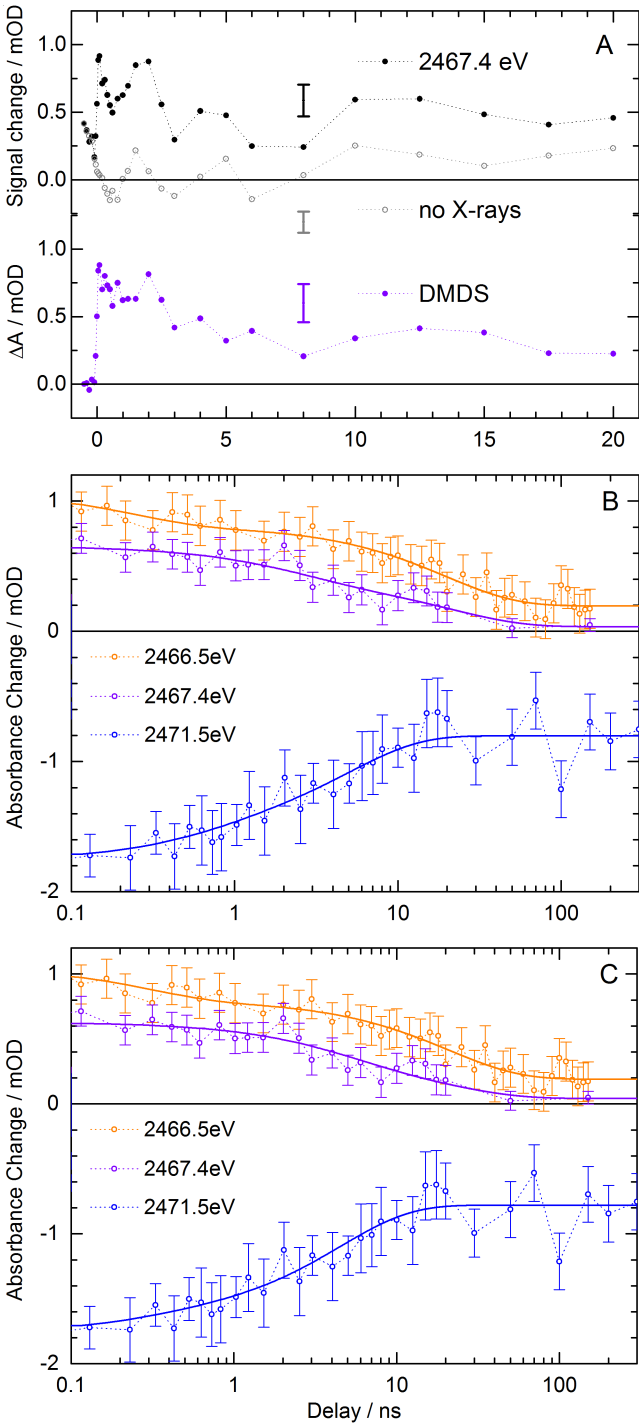

Figure S2. **A.** Differential pump-probe (black) and reference background (grey) scans of time delay (top panel). Background subtraction yields the molecular response of DMDS to the femtosecond laser excitation (purple trace, bottom panel). Error bars for each trace are indicated in the center of each panel. **B.** Biexponential decay models with individual time constants fit to each transient. **C.** Biexponential decay models with pairwise globally fit decay constants. The difference to individual fits is marginal. In either case, the weak subnanosecond component could be omitted without substantial fit degradation.

Table S1. Fit results for the model in Fig. S2B.

Model	ErfExp3 (User)			
Equation	y0+0.5*(1+erf((t-t0)/w*2*sqrt(ln(2))))*(A1*exp(-(t-t0)/t1) +A2*exp(-(t-t0)/t2) +A3*exp(-(t-t0)/t3) +A4)			
Reduced Chi-S				0.3078
Adj. R-Square				0.9838
		Value	Standard Erro	
2466.5eV	y0*	0	0	
	w*	70	0	
	t0*	2.73204	3.52061	
	t1	233.76825	144.2914	
	t2	3000	0	
	t3	19723.396	3730.63387	
	A1	0.2741	0.07242	
	A2	0	0	
	A3	0.61434	0.04206	
	A4	0.19513	0.02814	
2467.4eV	y0*	0	0	
	w*	70	0	
	t0*	2.73204	3.52061	
	t1	300	0	
	t2	2313.868	1688.18536	
	t3	21543.358	12739.00037	
	A1	0	0	
	A2	0.25994	0.12567	
	A3	0.35923	0.12672	
	A4	0.03563	0.02742	
2471.5eV	y0*	0	0	
	w*	70	0	
	t0*	2.73204	3.52061	
	t1	625.64175	1086.74568	
	t2	5058.7117	2122.67421	
	t3	20000	0	
	A1	-0.20317	0.23223	
	A2	-0.75686	0.23585	
	A3	0	0	
	A4	-0.80209	0.04157	

Table S2. Fit results for the model in Fig. S2C

Model	ErfExp3 (User)			
Equation	y0+0.5*(1+erf((t-t0)/w*2*sqrt(ln(2))))*(A1*exp(-(t-t0)/t1) +A2*exp(-(t-t0)/t2) +A3*exp(-(t-t0)/t3) +A4)			
Reduced Chi-S				0.2846
Adj. R-Square				0.9849
		Value	Standard Erro	
2466.5eV	y0*	0	0	
	w*	70	0	
	t0*	-0.36066	3.04017	
	t1*	285.20497	175.1817	
	t2*	4488.4208	963.55399	
	t3*	20972.138	3844.51981	
	A1	0.27023	0.07077	
	A2	0	0	
	A3	0.60802	0.0415	
	A4	0.19003	0.02753	
2467.4eV	y0*	0	0	
	w*	70	0	
	t0*	-0.36066	3.04017	
	t1*	285.20497	175.1817	
	t2*	4488.4208	963.55399	
	t3*	20972.138	3844.51981	
	A1	0	0	
	A2	0.29921	0.07589	
	A3	0.2875	0.0783	
	A4	0.04229	0.02292	
2471.5eV	y0*	0	0	
	w*	70	0	
	t0*	-0.36066	3.04017	
	t1*	285.20497	175.1817	
	t2*	4488.4208	963.55399	
	t3*	20972.138	3844.51981	
	A1	-0.12045	0.12184	
	A2	-0.86844	0.0772	
	A3	0	0	
	A4	-0.77897	0.04797	

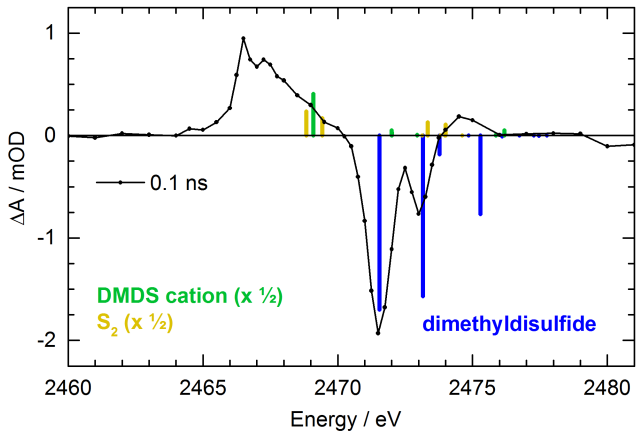

Figure S3. Differential absorbance as a function of X-ray photon energy at 0.1 ns after 267 nm excitation (black circles and solid line) and calculated X-ray transitions of the parent compound DMDS (shown in negative as absorption loss, the DMDS cation, and a disulfur molecule (S_2).

Possible cation formation

Formation of DMDS cations with a predicted dominant sulfur-1s transition in the same region as disulfur (**2**) as seen in figure S3 could in principle occur by two-photon absorption (TPA) during the τ = 100 fs excitation pulse at relatively high fluence of $\phi = 7 \cdot 10^{-16}$ ph/cm^2. A vertical ionization energy of 8.97 eV as well as an adiabatic ionization energy of 8.18 eV for DMDS have been measured by photoemission spectroscopy.[2,3] Both types of ionization do not allow for one-photon ionization at 267 nm (4.6 eV) while two-photon ionization can directly result in vertical ionization into the Frank-Condon region. Scaling of the TPA cross-sections with molecular weight[4] suggests that the TPA cross-section of DMDS has is less than $\sigma_2 = 8 \cdot 10^{-50}$ cm^4·s, amounting to $\sigma_2 \cdot \phi^2/\tau < 0.4\%$ TPA while linear DMDS absorption amounts to $\sigma_1 \cdot \phi = 8\%$ ($\sigma_1 = 1.1 \cdot 10^{-18}$ cm^2 equivalent to $\varepsilon_1 = 300$ M^{-1} cm^{-1} at 267 nm). This means that cation formation is negligible. We also note that power scans for other solvated molecular systems do not yield clear deviations form a linear response for threefold power compared to the power densities we have used.[5]

Relative yield analysis

To estimate the relative product yields and compare the time evolution from the differential spectra with the one extracted from the delay scans, we fitted Gaussian curves to the experimental data to quantify the contributions of the photoproducts as shown in Fig. S4. Each Gaussian represents the individual contribution of an associated sulfur species to the induced X-ray absorption. The area of each Gaussian normalized to the total area of induced absorption below 2470.5 eV at 0.1 ns divided by the calculated transition strength for each species provides an estimate of the relative yields. Figure S5 shows the temporal evolution of these relative yields. Clearly, these calculations depend upon the exact number of model components and the accuracy of the calculated transition strengths but they provide an idea of the product yield distribution.

The accuracy of the RASSCF calculations is only as good as the wavefunction modelling the quantum system. There is no agreed accuracy or precision for RASSCF calculations. Because S_2 is not a stable

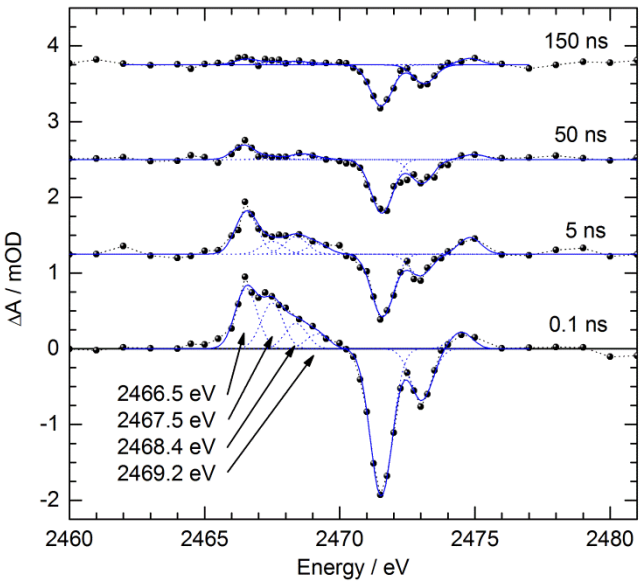

Figure S4. Differential spectra at the indicated delays between UV pump and X-ray probe pulses along with fits of 7 Gaussian lineshapes to the data to describe the observed transitions. The lineshape positions of the fit to the 0.1 ns spectrum (indicated for the lowest four Gaussians) where used in all subsequent spectra (5 ns to 150 ns). The areas of the normalized transitions below the ground-state bleaching signal, are plotted in Fig. S5.

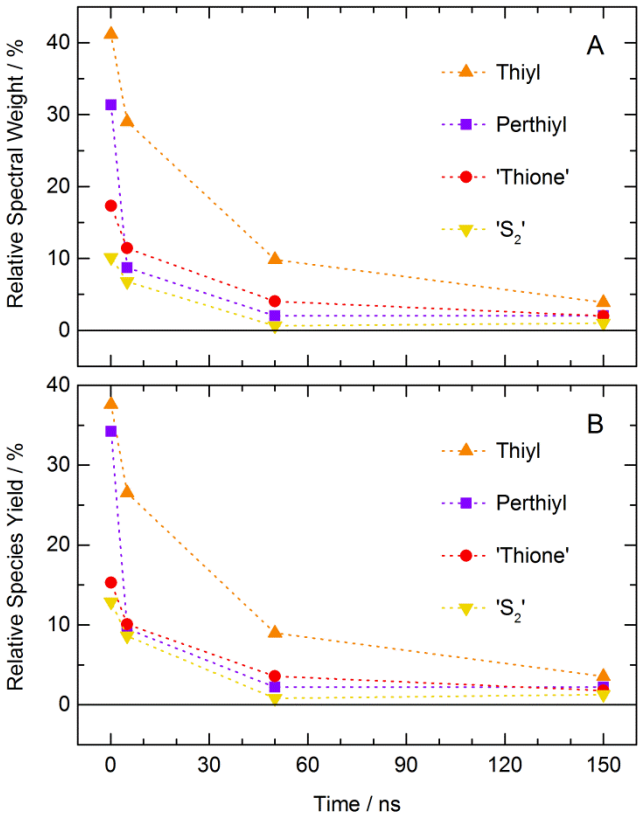

Figure S5. Contributions of the induced absorption components below the bleaching signal that have been fit to the data in Fig. S4. **A.** Spectral weights normalized to the sum of the four weights at 0.1 ns delay. **B.** Relative species yield, calculated from the data in panel A and RASSCF transition strengths in Fig. 2B.

species, experimental spectra to compare to are scarce. A publication by Rühl et al.[6] reports on induced absorption interpreted as the signature of S_2 which shows very good agreement in spectral position to our RASSCF predictions. The data suggests a weaker lowest transition strength compared to thiyl radicals as published recently by Sneeden et al[7] when taking into account the continuum absorption edge which is also reported in the same graphs. And sulfur K-edge absorption of DMDS is higher than the reported radical by Sneeeden et al.[7] Direct experimental comparison of thiyl and perthiyl radicals is difficult. Martin-Diaconescu and Kennepohl[8] used DFT-predicted transition strengths to extract yields from steady-state illumination of glutathione with X-rays with a ratio of calculated thiyl to perthiyl transition strengths of 1.6 while our calculations predict a ratio of 1.2.

From the data shown in Figure S5A we can deduce that the thiyl radical (**I**) pairs created by S-S bond cleavage are the spectrally dominant photoproduct. They make up about 40% percent of all induced absorption below the ground state bleaching signal 0.1 ns after photoexcitation. However, the relative species yields in Fig. S5B show that thiyl and perthiyl radicals exist in almost equal amounts at 0.1 ns after UV excitation. Since a radical pair is produced upon S-S bond cleavage, C-S bond cleavage is about twice more likely to occur than S-S bond cleavage. Assuming that all secondary products at 0.1 ns delay stem from perthiyl radicals (**II**), the quantum yield ratio for S-S bond cleavage vs. C-S bond cleavage is about 1:4 because nearly 40% (=2/5) thiyl radicals are observed at 0.1 ns (Fig. S5B), equating to about 1/5 probability of S-S bond cleavage whereas the other sulfur species would result from 4/5 probability for C-S bond cleavage.

Disulfur is not stable either and may combine with other disulfur molecules to form longer-lived sulfur clusters such as elementary sulfur (S_8). Both molecules feature considerably weaker resonant transitions[9] than the perthiyl radical which would not only explain the apparently faster perthiyl decay (see also Fig. S5) but the persistent ground state bleaching signal: While the spectral absorption edge is a quantative measure of the amount of sulfur in the probe beam, sulfur 1s→3p transitions vary considerably in strength among chemical species. Therefore, an irreversible product species with weaker sulfur 1s→3p transitions than DMDS will result a ground-state bleaching signal in differential pump-probe spectra during the transit time (≈100 µs) of the excited sample jet volume (flowing at about 3 µm/µs) across the probe beam. Furthermore, in principle all generated radicals may react with each other irreversibly in a diffusion-limited fashion, contributing to the loss of groundstate recovery.

Diffusion-limited product formation

At 150 ns, a bleach signal still persists, indicating incomplete groundstate recovery due to irreversible

reactions that prevent the reformation of groundstate DMDS molecules, e.g. the formation of tri- and tetrasulfide with lower absorption strength as discussed in the previous section. The formation of such products would be diffusion-limited as these are bimolecular reactions which require the encounter of two radicals. In order to estimate, whether it is feasible that such a process occurs during our observed time frame, we use two approaches to estimate diffusion-limited product yield. We estimate around 10% excitation efficiency, which amounts to 10 mM of excited DMDS molecules. This sets the length scale for bimolecular encounter to about 5 nm (as the cube root of inverse density of excited molecules). We can use the diffusion coefficient $D \approx 10^{-5}$ cm^2/s and the one-dimensional diffusion length

$$x = 2\sqrt{D \cdot t}$$

to calculate a mean diffusion time $t \approx 6$ ns from one excitation center to another. This places diffusion-limited reactions within our observed timeframe. Furthermore, we can use the approximation of a diffusion-limited rate constant

$$k = 4\pi D R_0$$

with R_0 as the sum of the effective radii of the two reactants R_A and R_B, typically around 0.5 nm for molecules such as the thiyl and perthiyl radicals, with $R_0 \approx 1$ nm. This leads to a diffusion-limited rate constant k which cannot exceed $8 \cdot 10^9$ L/mol·s. As discussed earlier, we estimate a 1:2 branching ratio between the thiyl and perthiyl radicals or estimated 10 mM thiyl and 5 mM perthiyl radical, respectively. If we calculate the possible formation of dimethyl tetrasulfide from two perthiyl radicals using the second order reaction kinetic equation

$$[A] = \frac{A_0}{(1 + 2k[A_0]t)}$$

for the bimolecular reaction

$$2A \rightarrow B$$

we obtain 0.4 mM concentration of perthiyl radicals at 150 ns, amounting to a detectable tetrasulfide concentration of 2.3 mM. Clearly, this estimate has limits, for instance, it only takes one of many possible reaction channels into account and assumes a very effective reaction of the two reactants. However, it demonstrates that diffusion-limited secondary reactions on the timescale of hundreds of nanoseconds can take place and are likely to contribute to differential spectra and persistent bleach signals of DMDS.

Energy calibration

A recent article on thiyl radical generation via X-ray ionization by Sneeden et al.[7] used a different energy calibration. To address this issue, we compared sulfur-1s absorption spectra of two compounds in Fig. S6 to relate our energy calibration to the other reported values. Sneeden *et al.* used a calibration at beamlines 4-3 and 6-2 at the Stanford Synchrotron Radiation Lightsource (SSRL) that is based on the sulfur-1s absorption spectrum of $Na_2S_2O_3$ measured by Sekiyama *et al.*[10] at the Photon Factory (PF) from

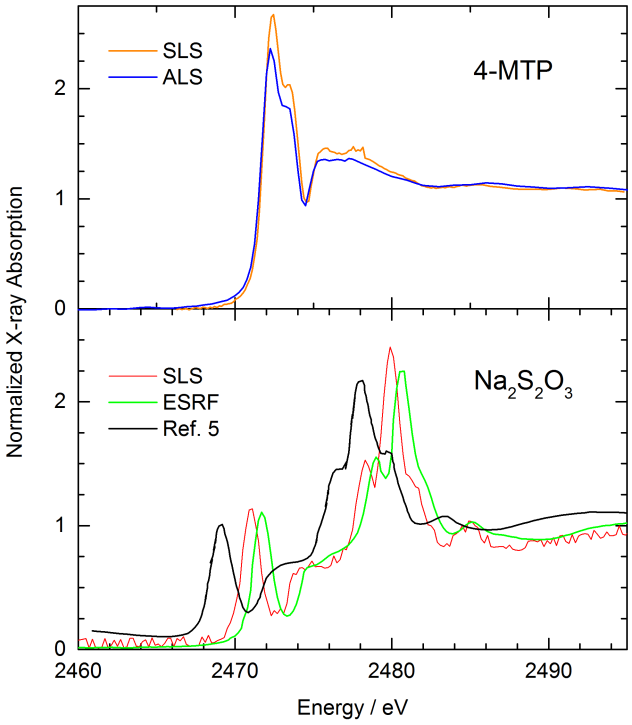

Figure S6. Sulfur-1s absorption spectra for calibration purposes. **A.** 4-methylthiophenol (4-MTP) as measured at the PHOENIX beamline of the Swiss Light Source (SLS) and at beamline 6.0.1 of the Advanced Light Source (ALS). **B.** Sodium thiosulfate from the SLS, the European Synchrotron Radiation Facility (ESRF) and as published in reference 10.

1986 which in turn bases its calibration on the sulfur-1s spectrum of NiS published in 1970.[11] Sneeden *et al.* report an energy position of the first peak of 4-MTP that is 1.6 eV lower than measured at beamline 6.0.1 of the Advanced Light Source (ALS), Berkeley, California, as shown in Fig. S6A.[1] In the same panel we also report the 4-MTP spectrum as measured at the PHOENIX beamline of the Swiss Light Source (SLS), Villigen, Switzerland, which is shifted by 0.1 eV to higher energy compared to the ALS spectrum. In panel B of the same figure the sulfur-1s absorption of $Na_2S_2O_3$ is shown as measured at the PHOENIX beamline, beamline ID21 of the European Synchrotron Radiation Facility (ESRF), Grenoble, France, and as reported by Sekiyama et al.[10]. The first absorption peak of $Na_2S_2O_3$ as published data of Sekiyama et al (black curve) lies about 2.0 eV below the one from at the SLS (red curve). The openly available spectrum of $Na_2S_2O_3$ from the ESRF (green curve) matches the SLS energy calibration more closely and is shifted by 0.7 eV to higher energy. We further note that the energy calibrations at the SLS and the ALS have been independently determined and are reproducible to within 0.5 eV. From this literature and calibration survey it is not clear what the best energy calibration is. It is therefore advisable to always report a spectrum that has been previously reported to allow other experimenters to compare their energy calibration to those of other beamlines and/or studies.

RASSCF calculations

As mentioned in the methods section of the main manuscript, the calculated sulfur-1s spectrum of DMDS (**1**) was shifted by -11.30 eV to match the experimentally obtained static spectrum of **1**. The subsequent transitions of all discussed species have also been shifted by the same amount to be comparable to the DMDS calculation results. Table S3 summarizes the nature of the dominant transitions for **1**, **I** and **II**. Table S4 shows all computed transition energies with applied relative shift and their respective transition strength for all discussed species.

Table S3. RASSCF-predicted dominant configurations of the lowest Sulfur-1s core-excited states.

Bound-Bound Transition	Contribution
DMDS (**1**)	
1s → LUMO	86.0%
1s → 50%(LUMO+1) +32%(LUMO+2)	82.0%
1s → LUMO+ 4	82.4%
Thiyl Radical (**I**)	
1s → SOMO	95.9%
Thiyl Radical (**I**)	
1s → SOMO	95.0%
1s → SOMO+ 4	93.7%

Table S4. Calculated transition energies and strengths for the discussed species.

Energy	Rel. Transition Strength
DMDS (**1**)	
2471.54683	7.38E-07
2471.54691	1.52E-10
2473.1544	3.36E-07
2473.15457	3.45E-07
2473.77669	2.87E-08
2473.77688	5.06E-08
2474.85568	1.12E-12
2474.85571	3.63E-14
2475.2931	7.92E-11
2475.29313	3.32E-07
2476.09315	3.30E-09
2476.09328	1.94E-12
2476.73188	3.59E-11
2476.73188	3.62E-11
2477.26906	2.86E-12
2477.26917	6.82E-13
2477.46476	2.61E-10
2477.46482	7.05E-10
2477.76042	3.22E-11
2477.76044	7.05E-14
Thiyl radical (**I**)	
2466.62773	3.87E-07
2474.02044	4.40E-08
2474.19552	1.11E-19
2474.3153	1.31E-08
2474.52031	7.49E-19
2474.55171	2.81E-08
2474.75928	3.17E-23
2474.77713	1.12E-09
2475.01398	2.90E-19
2476.21558	8.09E-16
2477.62179	7.55E-15
2477.86761	8.34E-14
Perthiyl radical (**II**)	
2467.2749	3.24E-07
2470.84358	1.57E-07
2471.51518	3.39E-08
2472.96255	1.32E-09
2473.32686	1.71E-17
2473.57301	3.89E-10
2473.94886	1.40E-12
2474.97154	1.20E-16
2475.09185	9.84E-09
2475.40339	1.82E-19
2475.41623	1.26E-10
2476.00463	5.16E-16
2476.13889	3.49E-12
2476.59315	5.21E-12
Energy	**Rel. Transition Strength**

Disulfur (**2**)	
2468.83159	1.39E-07
2468.88159	1.39E-07
2469.42218	1.00E-07
2469.42218	1.00E-07
2473.13808	3.21E-27
2473.33855	3.80E-28
2473.33953	1.53E-07
2473.79344	6.84E-30
2473.98009	4.09E-30
2474.00052	1.27E-07
2474.00302	5.79E-27
2474.61014	5.79E-29
Thioformaldehyde (**3**)	
2467.71157	4.01E-07
2472.74904	6.51E-10
2473.46097	2.08E-18
2474.05489	2.21E-10
2474.28872	2.97E-15
2474.43544	3.32E-09
2475.39878	2.43E-10
2476.26527	6.37E-24
2476.58041	4.84E-26
2477.95219	6.09E-16
HS radical (**III**)	
2465.11025	3.46E-07
2472.6256	1.60E-07
2472.63833	8.38E-09
2473.03377	1.21E-09
2473.05439	5.03E-11
2475.2771	3.04E-17
2477.99841	8.15E-12
2481.48876	1.70E-11
DMDS cation	
2469.08988	3.52E-07
2469.12561	1.29E-07
2471.99633	5.84E-08
2472.00425	3.49E-08
2472.93975	7.24E-09
2472.94403	1.02E-08
2475.85758	3.18E-09
2475.86669	1.14E-08
2476.17979	7.33E-09
2476.18346	6.17E-08

Bibliography of Supporting Information

(1) Ochmann, M.; von Ahnen, I.; Cordones, A. A.; Hussain, A.; Lee, J. H.; Hong, K.; Adamczyk, K.; Vendrell, O.; Kim, T. K.; Schoenlein, R. W.; Huse, N. *J. Am. Chem. Soc.* **2017**, *139*, 4789–4796.

(2) Wagner, G.; Bock, H. *Chem. Ber.* **1974**, *107*, 68–77.

(3) Borkar, S.; Sztáray, B.; Bodi, A. *J. Electron Spectrosc. Relat. Phenom.* **2014**, *196*, 165–172.

(4) Dragonmir, A.; McInerney, J. G.; Nikogosyan, D. N. *Appl. Opt.* **2002**, *41*, 4365–4376.

(5) Ogi, Y. et al. *Struct. Dyn.* **2015**, *2*, 034901.

(6) Rühl, E.; Flesch, R.; Tappe, W.; Novikov, D.; Kosugi, N. *J. Chem. Phys.* **2002**, *116*, 3316–3322.

(7) Sneeden, E. Y.; Hackett, M. J.; Cotelesage, J. J. H.; Prince, R. C.; Barney, M.; Goto, K.; Block, E.; Pickering, I. J.; George, G. N. *J. Am. Chem. Soc.* **2017**, *139*, 11519–11526.

(8) Martin-Diaconescu, V.; Kennepohl, P. *J. Am. Chem. Soc.* **2007**, *129*, 3034–3035.

(9) Hayter, C. E.; Evans, J.; Corker, J. M.; Oldman, R. J.; Peter Williams, B. *J. Mater. Chem.* **2002**, *12*, 3172–3177.

(10) Sekiyama, H.; Kosugi, N.; Kuroda, H.; Ohta, T. *Bull. Chem. Soc. Jpn.* **1986**, *59*, 575–579.

(11) Fujino, Y.; Sugiura, C.; Kiyono, S. *Technol. Rep. Tohoku Univ.* **1970**, *35*, 55.